Applied Catalysis B: Environmental 127 (2012) 36–46

Contents lists available at SciVerse ScienceDirect

Applied Catalysis B: Environmental

journal homepage: www.elsevier.com/locate/apcatb

# Catalytic activities of $Fe_2O_3$ and chromium doped $Fe_2O_3$ for sulfuric acid decomposition reaction in an integrated boiler, preheater, and catalytic decomposer

A.M. Banerjee [a], A.R. Shirole [a], M.R. Pai [a], A.K. Tripathi [a], S.R. Bharadwaj [a,*], D. Das [a], P.K. Sinha [b]

[a] Chemistry Division, Bhabha Atomic Research Centre, Mumbai 400085, India
[b] Powder Metallurgy Division, Bhabha Atomic Research Centre, Mumbai 400085, India

ARTICLE INFO

*Article history:*
Received 15 May 2012
Received in revised form 20 July 2012
Accepted 29 July 2012
Available online 3 August 2012

*Keywords:*
Hydrogen production
Sulfuric acid decomposition
Iron oxide
Chromium doped iron oxide
Granular catalyst
Redox

ABSTRACT

In our earlier work (Banerjee et al. [29]) we have reported the catalytic properties of powders of $Fe_{2(1-x)}Cr_{2x}O_3$ ($x = 0.0, 0.1, 0.2$) for sulfuric acid decomposition in a flow through quartz catalytic reactor with 2 g catalyst in presence of nitrogen as a carrier gas. With a practical application approach, in this work the two screened oxides, iron oxide and 10% chromium doped iron oxide, that showed good initial promise as catalyst for sulfuric acid decomposition were prepared in granular form and evaluated for sulfuric acid decomposition reaction using an indigenously developed dual tube quartz reactor which served as an integrated acid boiler, pre-heater, and decomposer. The effect of reaction variables, e.g., temperature, time, and acid flow rate on the catalytic activity was evaluated in detail employing 20 g of granular catalyst and 98 wt% $H_2SO_4$ (without any carrier/diluents gas). Temperature dependent catalytic activity results revealed that at lower temperatures (<775 °C) the Cr-doped sample showed much higher activity while at higher temperatures (~825 °C) the conversions levels were found to be similar on both the samples. No decrease in catalytic activity was observed for either catalysts during a 100 h catalytic run at 800 °C and at an acid flux of ~0.63 ml $min^{-1}$, but the chromium doped sample exhibited slightly higher activity over the entire time period. Both the catalyst exhibited a loss in catalytic activity when subjected to higher flow rates of sulfuric acid in the range 2–10 ml $min^{-1}$. The catalytic activities were correlated with the structure, morphology, redox, and thermal properties of the oxides by proper characterization of the fresh and the spent catalysts by XRD, FTIR, XPS, TPR, evolved gas analysis, and SEM. From the ex situ analysis of the spent catalyst samples the most probable mechanism of the high temperature sulfuric acid decomposition reaction was also proposed, which involves metal sulfate formation and decomposition steps. The enhanced catalytic activity of Cr-doped $Fe_2O_3$ was ascribed to lower thermal stability of its sulfate and better redox properties.



## 1. Introduction

The catalytic decomposition of sulfuric acid to produce sulfur dioxide, oxygen, and water is a topic currently gaining considerable importance as it can serve as the thermal to chemical energy conversion step in all the sulfur based thermochemical cycles. The sulfur based thermochemical cycles, e.g., the sulfur–iodine thermochemical cycle [1], the hybrid sulfur cycle [2], and the sulfur–bromine hybrid cycle [3] have been proposed for successful massive hydrogen production by splitting water [4–6]. Thermochemical cycles consist of a series of chemical reactions to produce hydrogen from water at much lower temperatures than required for the direct thermal decomposition of water [4–7]. The primary energy source to drive the cycle could be a renewable energy source such as nuclear [8] or solar heat [9,10]. Thus, hydrogen can be produced via these cycles without the use of fossil fuels that leads to the release of green house gases considered to be responsible for global warming.

Decomposition of sulfuric acid is the most endothermic reaction in the sulfur based thermochemical cycles and can be generally carried out at above 800 °C in a process reactor that can withstand high temperature heat from a nuclear reactor or a solar concentrator. The sulfuric acid decomposition comprises of the following two reactions in series:

$$H_2SO_4(g) = H_2O(g) + SO_3(g) \quad (\sim 450\,^{\circ}C) \tag{1}$$

$$SO_3(g) = SO_2(g) + 0.5O_2(g) \quad (\sim 800\text{–}900\,^{\circ}C) \tag{2}$$

* Corresponding author at: Fuel Cell Materials and Catalysis Section, 3-193 H, Chemistry Division, Modular Labs, Bhabha Atomic Research Centre, Mumbai 400085, India. Tel.: +91 22 25595100; fax: +91 22 25505151.
*E-mail address:* shyamala@barc.gov.in (S.R. Bharadwaj).

0926-3373/$ – see front matter © 2012 Elsevier B.V. All rights reserved.
http://dx.doi.org/10.1016/j.apcatb.2012.07.030

Sulfuric acid can be decomposed to its anhydride $SO_3$ with or without a catalyst, while the decomposition of $SO_3$ has been known to be a catalytic reaction. The catalyst efficiency, lifetime, and cost will play a significant role in determining the overall efficiency of the hydrogen production process [5,11].

The catalysts reported for sulfuric acid decomposition are mostly noble metal based such as ($Pt/Al_2O_3$, $Pt/TiO_2$, and $Pt/ZrO_2$) [12], ($Pt/TiO_2$ (rutile)) [13], ($Pt/BaSO_4$) [14], and theoretical studies on supported metal particles (Pd, Pt, Rh, Ir, and Ru supported on titania) [15]. JAERI used a catalyst bed of platinum [8] for sulfuric acid decomposition reaction in the closed cycle demonstration of the water-splitting iodine–sulfur process. However, the ever rising demand and increasing cost of noble metals make them less preferred for the above applications. Other reported issues with supported noble metals are the problems of leaching, sintering, and oxidation [13] of the metal particles during high temperature corrosive catalytic operation in sulfuric acid decomposition reaction. Substrate sulfation was also observed as a deactivation phenomenon for supported noble metals for the acid decomposition reaction by Norman et al. [16].

Metal oxide catalysts are cheap, easily available, and catalytically active and can be a substitute for noble metal catalysts as they fulfill the essential requirement of materials with better chemical, thermal stability, and modified catalytic properties. Simple binary oxides were first studied by Dokiya et al. [17] and Tagawa and Endo [18] but the order of activity of metal oxides were reported to be different. Barbarossa et al. [19] later on studied sulfuric acid decomposition over oxides samples of $Fe_2O_3$ and Pd–Ag alloy. Although simple oxide catalysts are active and can be a substitute for noble metal catalysts but their limitations of thermal instability, and sintering effects on repeated use, prevent them from the actual application. So an active as well as stable viable catalyst system still eludes us.

In recent years, focus has been laid on the synthesis of multimetal oxide systems to fulfill the essential requirement of chemical and thermal stability and improved catalytic properties. This subject is reviewed in several articles [20–23]. However, attempts toward mixed metal oxide systems for the sulfuric acid decomposition reaction, are very limited and have not been fully explored. Yannopoulos and Pierre [24] reported excellent catalytic activity of mixed metal oxides like $ZnFe_2O_4$ and $NiFe_2O_4$ for $SO_3$ decomposition reaction. Kim et al. [25] explored binary metal oxide catalysts based on iron (Fe/Al and Fe/Ti) and the catalytic activity of these catalysts increased with an increase in Fe loadings, indicating that the Fe component is active. Ginosar et al. [26] studied the efficiency of many mixed metal oxide catalysts for sulfuric acid decomposition namely $FeTiO_3$, $MnTiO_3$, $NiFe_2O_4$, $CuFe_2O_4$, $NiCr_2O_4$, $2CuO{\cdot}Cr_2O_3$, CuO, and $Fe_2O_3$. Very recently Machida et al. [27] reported the high catalytic activity of copper pyrovanadates for the above reaction. In this regard, the catalytic properties of three spinel ferrites $AFe_2O_4$ ($A = Cu^{2+}$, $Co^{2+}$, and $Ni^{2+}$) were investigated and reported by us, among which copper ferrite was the most promising catalyst by virtue of its superior redox properties and lower decomposition temperature of its sulfate [28]. We have also studied and reported the synthesis by conventional solid state reaction, physicochemical characterization, and catalytic activity evaluation of chromium doped iron oxide $Fe_{2(1-x)}Cr_{2x}O_3$ ($x = 0.0$, 0.1, 0.2) catalyst for the above application, where we found that 10% chromium doping helped in increasing the activity of iron oxide [29].

In the current study, the catalysts $Fe_2O_3$ and $Fe_{1.8}Cr_{0.2}O_3$ were prepared by co-precipitation in contrast to conventional solid state reaction used in our previous study [29], to obtain powders with better morphology. Besides, in almost all of the above studies the catalysts were employed in powder form and sulfuric acid vapors were passed over the catalyst along with a carrier gas. The preferred physical form of a practical heterogeneous catalyst used for gas phase reactions in industries in a fixed bed reactor is usually macroparticulate, i.e., consisting of granules or pellets of suitable size (3–25 mm) so that there is sufficient space between the particles for the gases to flow freely (minimum pressure drop across the reactor and at the same time minimum channeling or catalyst bypass) [5,30]. So, for a practical application approach, the two screened oxides that showed good initial promise as catalyst for sulfuric acid decomposition [29] – iron oxide and 10% chromium doped iron oxide, were investigated in granular form for the said reaction in an enhanced scale – using 20 g of catalyst. Catalytic activity was evaluated in absence of any carrier gas or diluents and under the flow of vapors of concentrated sulfuric acid (~98%) alone so that the catalytic decomposer operates in extreme conditions as posed in the actual reactor conditions. To ensure the above aspect, experiments were performed in an indigenously developed dual tube quartz reactor which served as an integrated boiler, pre-heater, and decomposer. Again, for practical purpose the chief criteria for a successful catalyst are (i) its ability to perform the task required of it efficiently under suitable conditions of pressure and temperature; (ii) its initial cost; and (iii) its life under operating conditions. So, the catalytic activity was evaluated as a function of reaction variables, e.g., temperature, time, and acid flow rate to completely assess the catalytic performance. Subsequently, the spent catalyst sample was analyzed ex situ by physicochemical and spectroscopic techniques to understand the reaction mechanism and investigate any deactivation phenomenon which might be occurring at the molecular level.

## 2. Experimental

### 2.1. Preparation

$Fe_2O_3$ and $Fe_{1.8}Cr_{0.2}O_3$ catalyst spherical granules were prepared by co-precipitation method. The step by step procedure for the synthesis of the granular catalyst is illustrated in Scheme 1. Calculated amounts of nitrate precursors of iron (III) and chromium (III) were dissolved separately in deionized water. To prepare the doped material the two solutions were mixed together while in case of $Fe_2O_3$ only ferric nitrate was used. Dilute aqueous ammonia was gradually added drop wise to the aforementioned solutions under vigorous stirring until precipitation was complete (pH 8.5). The precipitate thus obtained were further aged overnight and filtered off. The resulting cakes were oven-dried at 100 °C for 12 h and then shaped into spherical beads of 4–6 mm in diameter using polyvinyl alcohol as a binder. Finally the spherical granules were calcined at 750 °C for 12 h in air which also ensured complete removal of the binder. The heating and cooling rates were maintained at 5 °C/min.

### 2.2. Characterization

Powder XRD patterns for the synthesized samples and the spent catalyst samples were recorded in $2\theta$ range of 10–70° (step width 0.02° and step time 1.25 s) using a powder X-ray Diffractometer (Philips, model 1729) equipped with nickel filtered Cu Kα radiation. The crystallite size $D$ was calculated from XRD line width according to the Scherrer equation:

$$\Delta(2\theta) = \frac{K\lambda}{D(\cos\theta)} \quad (3)$$

where $\Delta(2\theta)$ is the width at half-maximum intensity (in radians) and $\theta$ is the Bragg angle of the (2 0 3) plane in the diffraction pattern of the peak, $K$ is a constant, depending on the line shape profile (currently $K = 0.9$), $\lambda$ is the wavelength of the X-ray source (in the case of Cu radiation, $\lambda = 0.154059$ nm), and $D$ is the crystallite size in

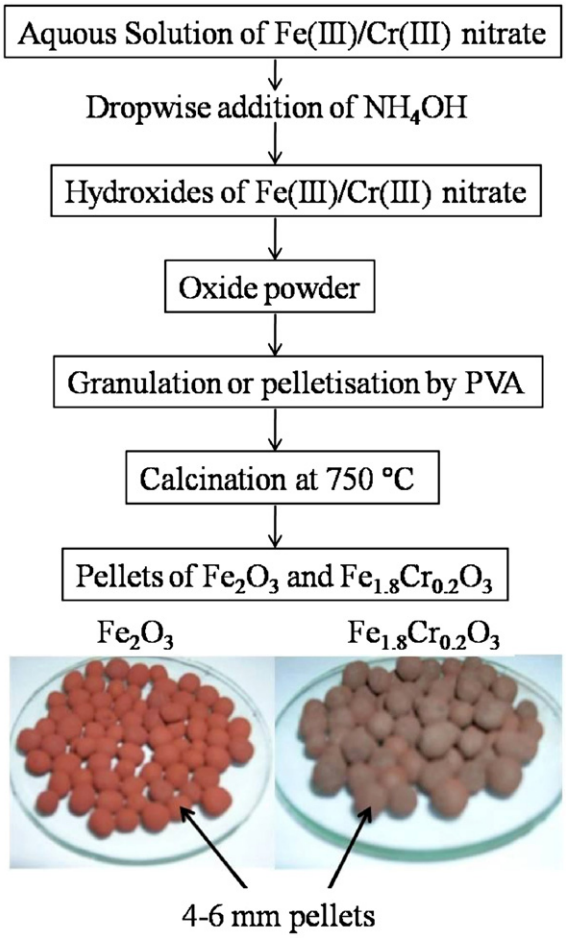


**Scheme 1.** Flow chart for the preparation of $Fe_2O_3$ and $Fe_{1.8}Cr_{0.2}O_3$ catalyst granules.

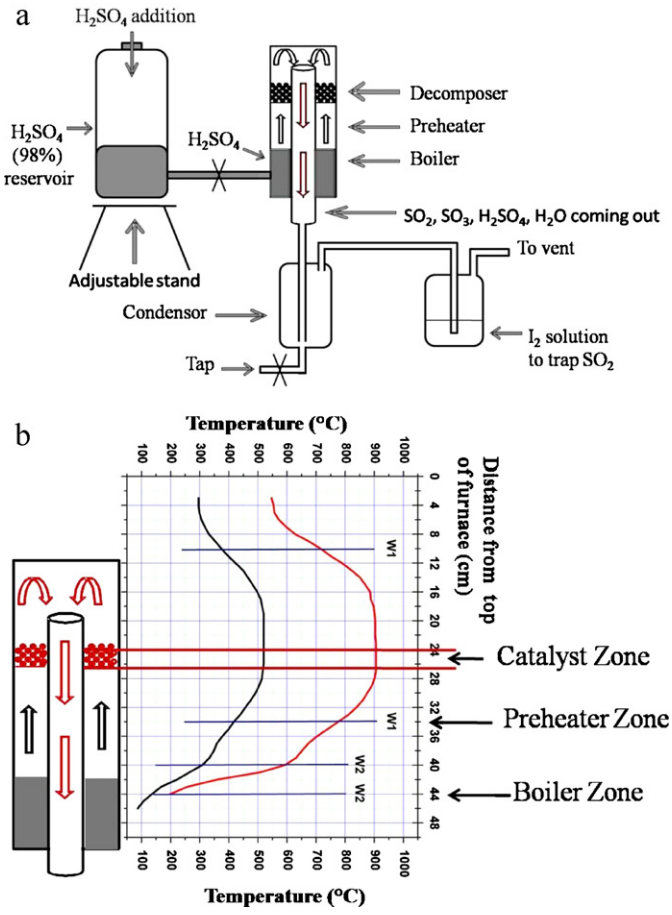


**Fig. 1.** (a) Block diagram of the enhanced scale quartz experimental set up for carrying out sulfuric acid decomposition reaction with 20 g granular catalyst. The annular space in dual quartz tube reactor serves as the integrated boiler, superheater, and decomposer for $SO_2$. (b) The temperature profile is on the surface of the reactor by setting the catalyst zone temperature at 550 °C (black line) and 950 °C (red line) and the acid zone at 200 °C and 350 °C respectively. (For interpretation of the references to color in this figure legend, the reader is referred to the web version of the article.)

nm. A Quantachrome Autosorb-1 analyzer was employed for measurement of BET surface area by recording the nitrogen adsorption isotherms. The FTIR spectra of the solid samples were recorded in KBr using a Jasco FTIR (model 610) in range of 400–4000 $cm^{-1}$ with a resolution of 4 $cm^{-1}$. Redox behavior of the oxide sample toward reduction oxidation cycles was studied by recording temperature programmed reduction/oxidation (TPR/TPO) profiles on a TPDRO-1100 analyzer (Thermo Quest, Italy) under the flow of $H_2$ (5%) + Ar, alternatively, $O_2$ (5%) + He gas mixtures at a flow rate of 20 ml $min^{-1}$, in temperature range of 25–1000 °C for TPR and up to 800 °C for TPO at a heating rate of 6 °C/min. The samples were pretreated at 350 °C for about 2.5 h in helium, prior to recording of the first TPR run. The morphological features were analyzed by a Scanning Electron Microscope (Mirero, Korea, model-AIS2100). Prior to SEM examination, the samples were coated with a thin gold layer (~150 Å thick) so as to avoid the problem associated with charging. To analyze the surface elemental composition and valence state of ions in the catalysts, X-ray photoelectron spectroscopy (XPS) was employed. A Thermo VG Clamp2 Analyzer based spectrometer using a radiation source of Mg Kα radiation (1253.6 eV, 30 mA × 8 kV) was used for these studies. As an internal reference for the absolute binding energy, a C 1s peak of 284.6 eV was used. To understand the nature of stable species produced on the catalyst during decomposition of sulfuric acid, the spent catalyst samples were heated in the temperature range of 400–1000 °C at a heating rate of 10 °C/min and the evolved gases were analyzed by a QMS coupled to a TG-DTA (model-SETSYS Evolution-1750, SETARAM).

### 2.3. Catalytic activity

Sulfuric acid decomposition reaction was carried out in an experimental set-up shown schematically in Fig. 1a. The set-up consists of a sulfuric acid reservoir, a dual tube quartz catalytic reactor, condenser for unreacted sulfuric acid, and a trap for analyzing one of the products $SO_2$. The level of acid in the reservoir was kept constant throughout the experiments by adding sulfuric acid (~98 wt%) continuously using a burette. The quartz catalytic reactor consists of dual quartz tubes, with sulfuric acid accumulating at the bottom of the annular region and 20 g of catalyst at the top of the annular region and held on its position by a perforated quartz disc. The upper level of the acid in the annular zone remains constant as per the height of acid in the reservoir. The acid zone and the catalyst zone were heated separately by a two-temperature zone electric furnace while temperatures of the two zones were controlled by the thermocouples held on the surface of the quartz reactor. Temperature profiles on the reactor surface were obtained by setting different temperatures of the acid zone (250–325 °C) and catalyst zone (550–950 °C). A typical temperature profile on the surface of the reactor on setting the catalyst zone temperature at 550 °C and 950 °C with acid zone temperatures at 200 °C and 350 °C, respectively, is shown in Fig. 1b. As seen from the temperature profile, the region in between the acid zone and catalyst zone acted as a

pre-heater region where temperature increased gradually from the former to later zone thus minimizing acid condensation.

To study the time dependent catalytic activity for 100 h, the acid zone was heated to temperature of ~325 °C and the catalyst region was heated to temperature of 800 °C. This temperature of acid zone ensured an almost constant acid flux of ~0.63 ml $min^{-1}$ of liquid sulfuric acid as a feed to the decomposition zone corresponding to a GHSV of ~800 ml $g^{-1}$ $h^{-1}$ (WHSV of ~3.4 g acid $g^{-1}$ catalyst $h^{-1}$). The sulfuric acid accumulated at the annular region of the dual quartz tube on attaining temperatures near to its boiling point (~334 °C) evaporated and reached the catalyst zone passing through the annular area in between the boiling and catalyst zone. In this zone in between the acid and catalyst zone in the annular region of the dual quartz tube, sufficient high temperatures were achieved to dehydrate $H_2SO_4$ to $SO_3$ (Eq. (1)). $SO_3$ then passed through the catalyst bed held at a higher temperature undergoing decomposition (Eq. (2)). This new design based on dual quartz tube can function as an integrated acid boiler, preheater, and decomposer. This concept of a dual tube integrated catalytic reactor has no high temperature connections and so renders it free from acid corrosion and leakage, a challenging issue in successful operation of sulfuric acid decomposition reaction [31,32]. This type of reactors will be particularly useful for coupling with bayonet type heat exchangers, which are employed for high temperature reactions like selective catalytic reduction (SCR) [33,34], coal gasification [35]. In fact, theoretical studies as well as experiments to measure heat exchange efficiencies of bayonet type heat exchangers have already being carried out for sulfuric acid decomposition recently by Nagarajan et al. [36,37] and Ma et al. [38,39]. Thus, successful operation of catalytic sulfuric acid decomposition in an integrated acid boiler, preheater, and decomposer – dual tube quartz reactor for more than 100 h in our experiments will provides deep impetus in extending this concept to large scale catalytic reactor design and fabrication for bench scale demonstration experiments of sulfur based thermochemical cycles.

During a typical temperature dependent catalytic run, the temperature of the catalyst zone was varied from 725 to 825 °C in step wise increments of 25 °C. The feed composed of sulfuric acid vapors of a constant flux generated by heating the acid boiler region at a constant temperature. The product analysis was done by chemical titrimetric method, the unreacted sulfuric acid being titrated after condensation and one of the products $SO_2$ was measured by trapping it in $I_2$ solution. Blank experiments verified that homogeneous vapor phase reactions did not occur under these conditions.

In addition to the time dependent and temperature dependent catalytic activity, effect of variation of flux of sulfuric acid on the catalytic activity was also investigated. The sulfuric acid flux was varied by adjusting the temperature of the boiling zone of the integrated reactor. A post reaction ex situ characterization of the spent catalyst was performed to check the structural/morphological integrity, presence of any stable intermediates resulting in deactivation of the catalysts, and to predict the most probable mechanism of the acid decomposition.

## 3. Results and discussion

The decomposition of sulfuric acid is a highly endothermic reaction and occurs only at very high temperatures. The temperature dependent catalytic activities for the decomposition of sulfuric acid over pristine iron oxide and chromium doped iron oxide catalysts are shown in Fig. 2a. Both the pristine and doped iron oxide samples were found to be active for decomposition of sulfuric acid in temperature range of 700–825 °C. Catalytic activity of both the samples increased with rise in temperature. At lower temperatures (<775 °C) the catalytic activity of the doped sample is found to be much higher than the pristine $Fe_2O_3$. But, at higher temperatures (>775 °C) the activity of the two oxides increases in a similar manner with the doped catalyst being more active. The $SO_2$ yield as measured with chemical titrimetric method increased with rise in temperature with a maximum activity of ~76% and ~82% for $Fe_2O_3$ and $Fe_{1.8}Cr_{0.2}O_3$ at ~825 °C. The equilibrium product yield theoretically calculated is indicated in red curve in Fig. 2A. The experimental points for the doped catalysts are close to equilibrium above 750 °C. It is pertinent to mention here that no $SO_2$ was produced under identical conditions in absence of a catalyst.

The time dependent product yield of $SO_2$ obtained in the experiments that lasted for 100 h is shown in Fig. 2B. It is evident from the figure that there is no deterioration in the catalyst performance during 100 h run at a sulfuric acid flux of ~0.63 ml $min^{-1}$ for both the samples. So, the catalysts are stable under the experimental conditions of high temperature and highly corrosive reactants and products. This result implies that these catalysts are active during prolonged use under acidic environment. However the $SO_2$ yield was higher for the Cr doped samples (also close to equilibrium yield) than the pristine $Fe_2O_3$ throughout the 100 h run at 800 °C.

The effects of sulfuric acid flux on the product yield are shown in Fig. 2C (0.2–1 ml $min^{-1}$) and Fig. 2D (1–10 ml $min^{-1}$). From Fig. 2C it is evident that at a lower flux in the range of 0.2–1 ml $min^{-1}$ $H_2SO_4$ the decomposition rate decreases linearly with a small slope. Further from 1 to 2 ml $min^{-1}$ the product yield decreases with a greater slope but when the acid flux crosses 2 ml $min^{-1}$ a drastic decline in the product yield is noticed. These reductions in $SO_2$ yield may be attributed to the decrease in contact time between the reactant sulfuric acid vapors and the catalyst.

After the time dependent experiments for 100 h were over the spent catalyst granules were collected and analyzed for any obvious change in structure, morphology, or oxidation states than the unused ones. The analysis of the fresh and spent catalyst along with the catalytic activity results were taken into account to predict the most probable mechanism of sulfuric acid decomposition and also the reason for improved performance of the Cr doped catalyst.

Fig. 3 shows the XRD patterns of the fresh and spent catalyst samples. The XRD pattern of pristine and Cr-doped $Fe_2O_3$ ($Fe_{1.8}Cr_{0.2}O_3$) prepared by co-precipitation method matches with the JC-PDS card No. 33-0664 corresponding to Hematite, α-$Fe_2O_3$. From the comparison of the XRD patterns of the oxide samples from Fig. 3, it is evident that even after exposure of the catalyst for 100 h in sulfuric acid stream at 800 °C there is no obvious change in phase or formation of any additional phases for both the samples. Thus we can conclude that the catalyst is having sufficient phase stability even after exposure to harsh catalytic reaction environment for sufficiently long duration. Table 1 lists the lattice parameters, crystallite size from Scherrer equation, BET surface area of the fresh and used $Fe_2O_3$ and $Fe_{1.8}Cr_{0.2}O_3$ catalyst samples. The BET surface area of the two fresh catalysts ($Fe_2O_3$ ~17 $m^2$ $g^{-1}$ and $Fe_{1.8}Cr_{0.2}O_3$ ~18 $m^2$ $g^{-1}$) are comparable. The decrease in BET surface area on catalytic use for sulfuric acid decomposition reaction at high temperature, of both the pristine and doped catalysts can mostly be attributed to sintering and surface sulfate formation. The increase in crystallite size of both the used samples as compared to the fresh catalysts can be probably ascribed to particle agglomeration due to the sintering effect on exposure of the catalyst granules at high temperature of 800 °C for 100 h. The lattice parameters and cell volume of all the samples were generated from Powder Indexing programme [40]. The ionic radii of iron and chromium are very similar: 0.067 nm for $Fe^{3+}$ and 0.064 nm for $Cr^{3+}$ [28,41] and their oxides are iso-structural with rhombohedral crystal structure. The structure of α-$Fe_2O_3$, α-$Cr_2O_3$ comprises of a hexagonal close packed array of oxygen ions with Cr and/or Fe ordered on two-thirds of the octahedral interstices giving rise to eight cations in the first neighbor sphere. From Table 1 it is evident that the lattice parameters of

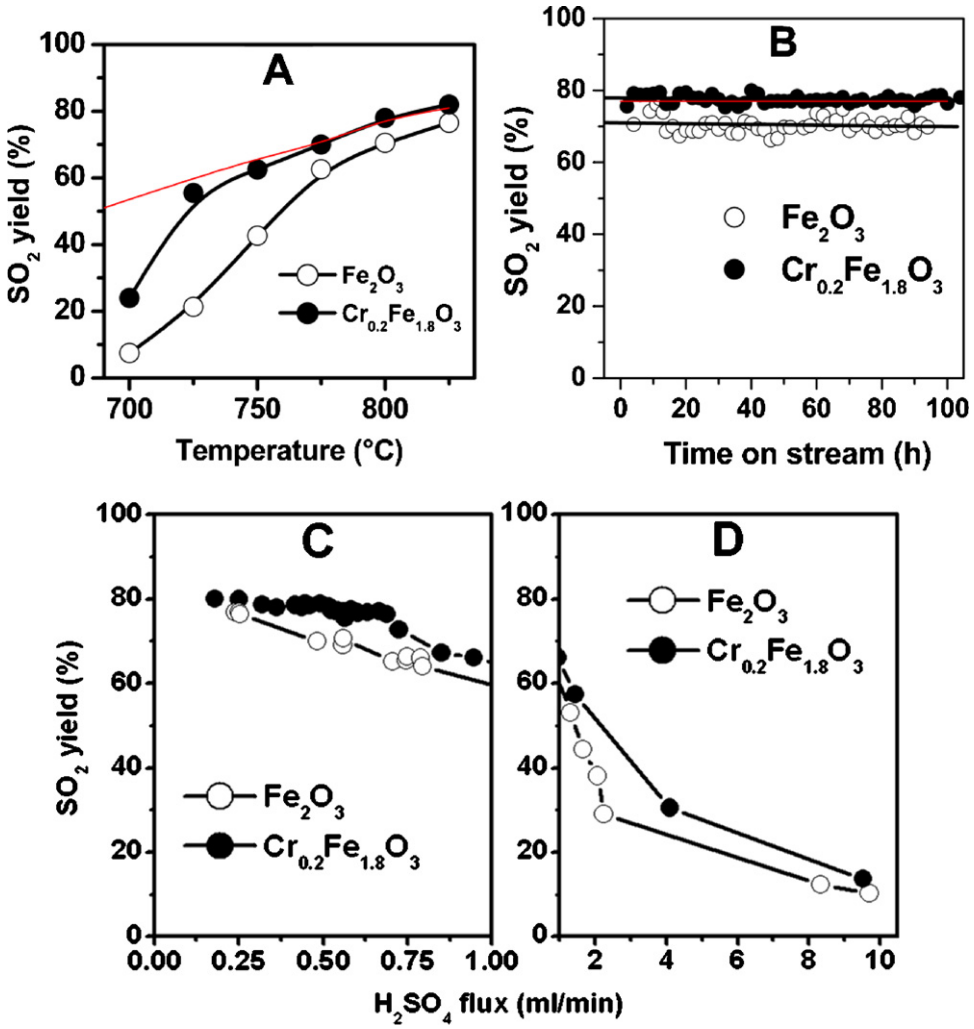


**Fig. 2.** The catalytic activities of $Fe_2O_3$ and $Fe_{1.8}Cr_{0.2}O_3$ (20 g catalyst) for sulfuric acid decomposition; (A) temperature dependent catalytic activities at a $H_2SO_4$ flux of ~0.63 ml $min^{-1}$ (WHSV of ~3.4 g acid $g^{-1}$ catalyst $h^{-1}$); (B) catalytic activity for 100 h time on stream at 800 °C at a $H_2SO_4$ flux of ~0.63 ml $min^{-1}$ (WHSV of ~3.4 g acid $g^{-1}$ catalyst $h^{-1}$); (C and D) the effects of sulfuric acid flux on the product yield at 800 °C. The calculated equilibrium product yields are shown in red in (A and B). (For interpretation of the references to color in this figure legend, the reader is referred to the web version of the article.)

$Fe_2O_3$ are in well agreement with those listed in the JC-PDS card No. 33-0664 corresponding to Hematite, α-$Fe_2O_3$. On $Cr^{3+}$ doping at $Fe^{3+}$ sites there is a slight decrease in lattice parameters of $Fe_{1.8}Cr_{0.2}O_3$ than $Fe_2O_3$ due to a minor decrease in ionic radii of the substituting ion.

Fig. 4 shows the X-ray photoelectron spectroscopy (XPS) spectrum of the core level Fe 2p in the fresh and spent $Fe_2O_3$ catalysts. The binding energy (B.E.) of the Fe $2p_{3/2}$ in the fresh sample was determined to be 710 eV while it was observed at higher B.E. value of 711.1 eV on spent catalyst. This suggests that Fe is present in $Fe^{3+}$ state [42] in both the fresh and used iron oxide catalysts, but due to formation of some surface sulfate species a shift toward higher binding energy is noticed in the spent catalyst. The XPS spectra were also recorded for the O 1s region of the iron oxide catalyst before and after catalytic activity cycle and are presented in Fig. 5. The O 1s peak as shown in Fig. 5, exhibits a shift in the higher binding energy region from 529.35 to 530.28 eV. This shift toward higher binding energy can be attributed to oxygen present in a surface sulfate species [43]. However, a more accurate assessment of the presence of sulfates in the surface can be obtained using the sulfur 2p spectra [44] shown in inset of Fig. 5. We observe a prominent peak at 169 eV which is specific for sulfur present as sulfates [42]. These results from XPS study of this sample indicate that the catalyst itself is very stable even after 100 h of reaction with no change

**Table 1**
Lattice parameters, crystallite size, and BET surface area of the catalyst samples.

| Sample | *a* (nm) | *b* (nm) | *c* (nm) | Volume ($nm^3$) | Crystallite size (Scherrer equation) (nm) | BET surface area ($m^2\ g^{-1}$) |
|---|---|---|---|---|---|---|
| $Fe_2O_3$ JCPDS card no.33-0664 | 5.035 | 5.035 | 13.74 | 301.93 | – | – |
| $Fe_2O_3$ fresh | 5.02879 | 5.02879 | 13.74658 | 301.060 | 49.5 | 17 |
| $Fe_2O_3$ used | 5.03969 | 5.03969 | 13.74633 | 302.361 | 66.5 | 13 |
| $Fe_{1.8}Cr_{0.2}O_3$ fresh | 5.03276 | 5.03276 | 13.70485 | 300.619 | 46.5 | 18 |
| $Fe_{1.8}Cr_{0.2}O_3$ used | 5.03560 | 5.03560 | 13.69734 | 300.794 | 74.4 | 3 |

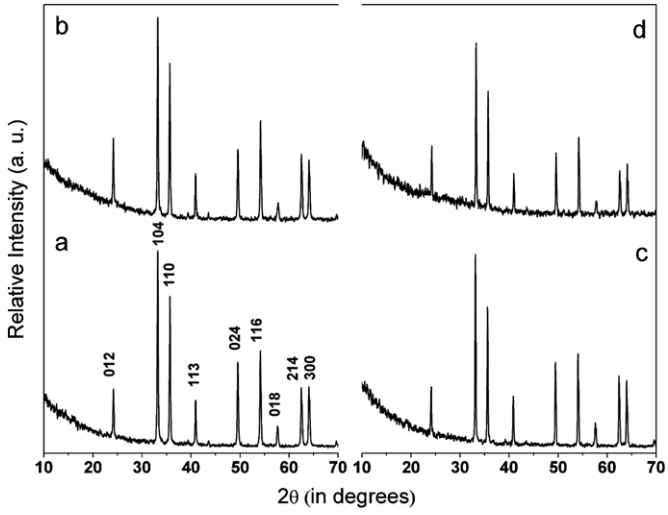


**Fig. 3.** The XRD pattern of the fresh (a) $Fe_2O_3$ and (b) $Fe_{1.8}Cr_{0.2}O_3$ catalysts which indicates the formation of solid solution of 10% chromium in $Fe_2O_3$ lattice. The (c) spent $Fe_2O_3$ and (d) spent $Fe_{1.8}Cr_{0.2}O_3$ catalysts does not show any phase change or formation of any additional phases.

in the valence state of Fe [45] but some surface sulfate species are present on the used catalyst.

Infrared spectroscopy can be used to monitor chemical and structural changes in the mixed metal oxides. A comparison of the FTIR spectra of the fresh and spent catalyst samples is shown in Fig. 6. The prominent infrared absorption bands ($cm^{-1}$) observed for fresh $Fe_2O_3$ catalyst are at 470 $cm^{-1}$ and 540 $cm^{-1}$ with a well pronounced shoulder at 591 $cm^{-1}$. McDevitt and Baun [46] published the characteristic infrared bands of hematite at 560, 480, 370, and 325 $cm^{-1}$. Schwertmann and Taylor [47] suggested the characteristic bands at 540, 470, and 345 $cm^{-1}$ in the low frequency region can be used as fingerprints in the identification of hematite. Since our measurements were made in between 400 and 4000 $cm^{-1}$, we could not record the lower wave number peaks. But, peaks at 479 $cm^{-1}$ and 560 $cm^{-1}$ in $Fe_2O_3$ are in good agreement

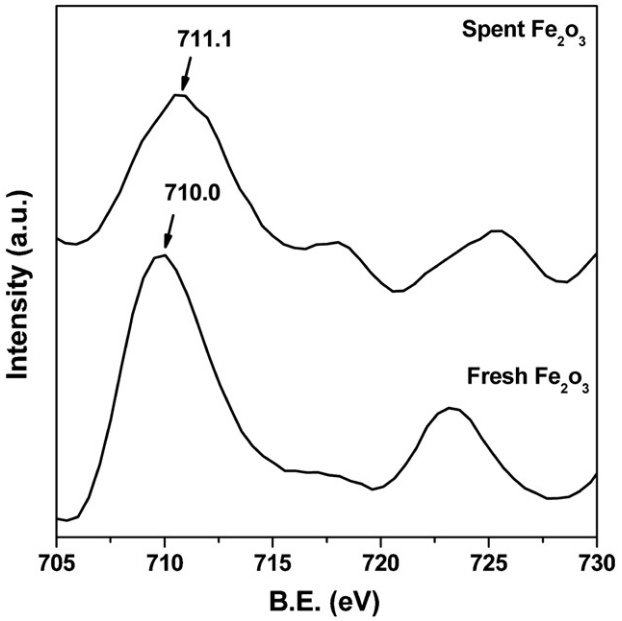


**Fig. 4.** Fe-2p X-ray photoelectron spectra (XPS) of the fresh $Fe_2O_3$ before reaction and of used $Fe_2O_3$ collected after 100 h use in high temperature sulfuric acid decomposition reaction.

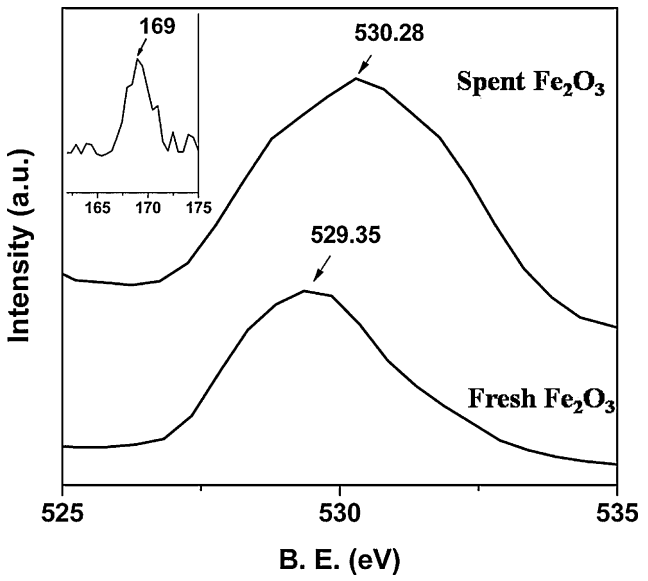


**Fig. 5.** O-2p core level X-ray photoelectron spectra (XPS) of fresh and used $Fe_2O_3$ samples. Inset is shown the peak at 169 eV due to the presence of sulfates (oxidation state of sulfur, +6) in the sample.

with hematite structure, the higher wave number peak being due to Fe—O bond stretching and the lower one due to Fe—O—Fe deformation [48,49]. In the chromium doped sample ($Fe_{1.8}Cr_{0.2}O_3$) the peak positions are slightly shifted toward higher wave number region and appear at 575 $cm^{-1}$ and 493 $cm^{-1}$ along with a shoulder at 457 $cm^{-1}$. The shift marks the microstructural defects generated

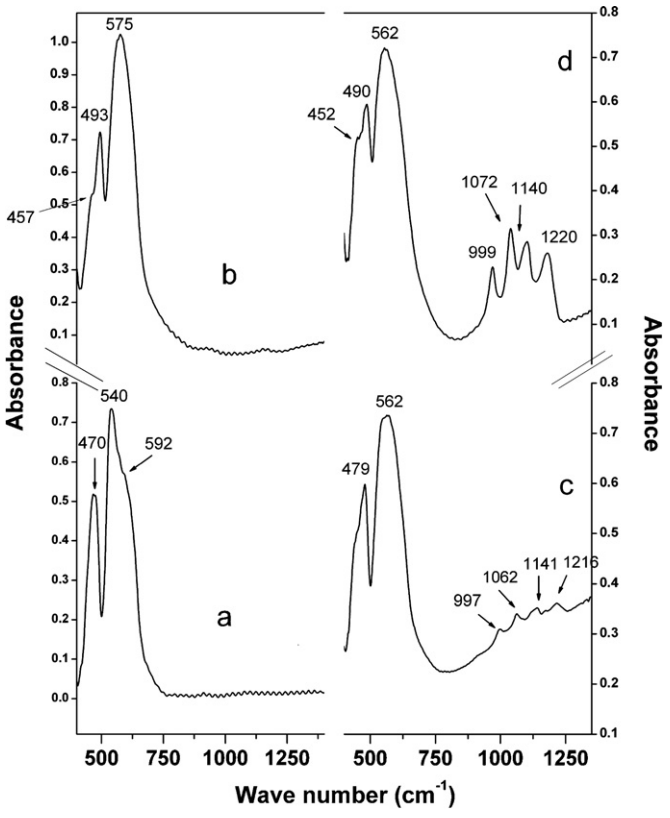


**Fig. 6.** The FTIR spectra of the fresh $Fe_2O_3$ and $Fe_{1.8}Cr_{0.2}O_3$ catalysts are shown in spectra a and b respectively. The FTIR spectra of the (c) spent $Fe_2O_3$ and (d) spent $Fe_{1.8}Cr_{0.2}O_3$ catalysts show four peaks in the 900–1250 $cm^{-1}$ region which are characteristic of SO stretching vibrations of bidentate metal sulfates.

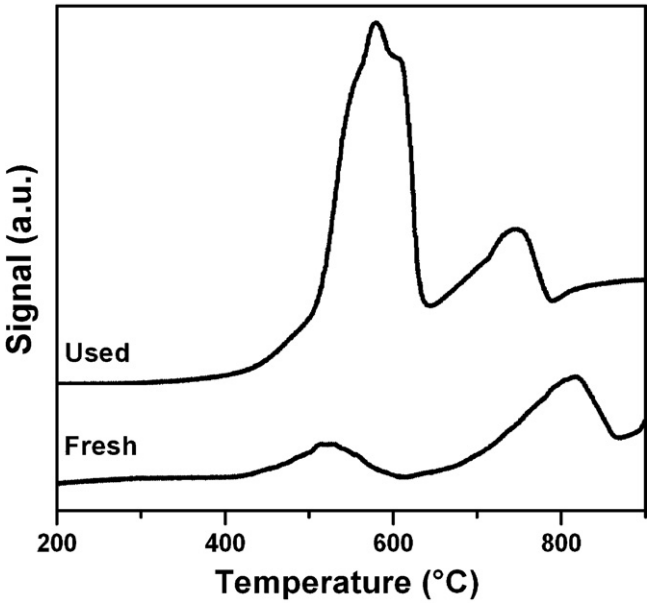


**Fig. 7.** Temperature programmed reduction profile of the fresh and used $Fe_2O_3$ catalysts.

in the structure of the iron oxide as a consequence to Cr doping. Also, since Cr is substituted at Fe sites, Cr—O—Fe bonds will be present in addition to Fe—O—Fe bonds, thus decreasing the reduced mass and consequently increasing the peak position, as the IR wave number and reduced mass are inversely related. Further, all the peak positions in the 400–600 $cm^{-1}$ region are altered in the used samples as compared to the corresponding fresh ones indicating changes in the microstructure on catalytic use. To further stress upon this fact, we can observe from Fig. 6 that additional peaks appear at the range of 1000–1250 $cm^{-1}$ in both the spent catalysts which can be assigned to SO bond stretching in metal sulfates. Formation of ferric sulfate was confirmed by XPS but information about the structure of the surface sulfate species was obtained from FTIR spectra of the spent catalyst samples. The spent $Fe_2O_3$ catalyst exhibited characteristic small peaks at 997, 1062, 1141, and 1216 $cm^{-1}$, while the spent $Fe_{1.8}Cr_{0.2}O_3$ exhibited peaks at 999, 1072, 1140, and 1220 $cm^{-1}$ (Fig. 6), indicative of $C_{2v}$ symmetry and bidentate sulfate coordination, because a clear distinction between monodentate and bidentate coordination can be made, based on the number of observed bands (monodentate, $C_{3v}$, with three bands, and bidentate, $C_{2v}$, with four bands) [28,50]. The peaks arise due to SO bond stretching in metal sulfates with the lowest wave number peak assigned to $\upsilon_1$ stretching mode while the higher three peaks are due to $\upsilon_3$ mode. Sulfur–oxygen double bonds (i.e., SO) show a strong absorption band at 1381 $cm^{-1}$ [51]. Thus, the FTIR spectra of the spent catalyst samples confirm the presence of sulfates and that the sulfates are consistent with bidentate coordination. These metal sulfates are probably the transient intermediates of sulfuric acid decomposition to sulfur dioxide over these metal oxide catalyst. We can also observe from Fig. 4 that the intensity of the FTIR peaks for the sulfate species in the 950–1250 $cm^{-1}$ region, is more on the doped catalysts indicating the presence of sulfates in higher amounts in $Fe_{1.8}Cr_{0.2}O_3$ than $Fe_2O_3$.

The temperature programmed reduction profile of the fresh and spent $Fe_2O_3$ catalysts is shown in Fig. 7. The TPR profile of fresh sample comprises of a prominent band with $T_{max}$ at ~520 °C and another broad band with onset temperature of 615 °C and having $T_{max}$ at ~815 °C due to the reduction of $Fe^{3+} \rightarrow Fe^0$ species in three reduction steps: $Fe_2O_3$ to $Fe_3O_4$, $Fe_3O_4$ to FeO and finally FeO to Fe metal as shown in Eqs. (4)–(6) [28,52]. In these samples the second

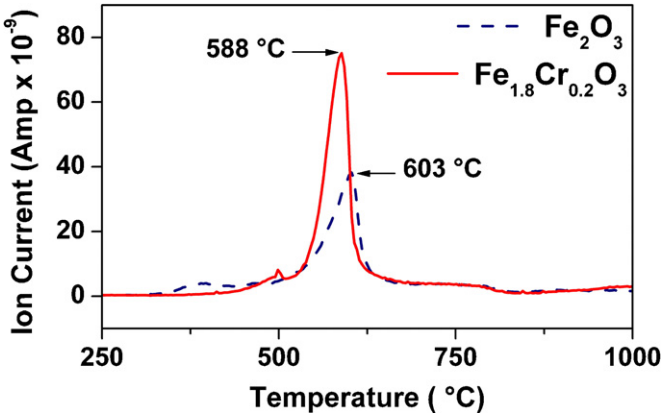


**Fig. 8.** Evolved gas analysis for mass no. 64 in mass spectrometer as a function of temperature of the spent $Fe_2O_3$ and $Fe_{1.8}Cr_{0.2}O_3$ catalysts post 100 h performance in sulfuric acid decomposition reaction.

and third peaks merge together to give a broad band at ~815 °C. In case of spent $Fe_2O_3$ sample the reduction profile also shows a two step profile but the first peak is of reasonably higher intensity with $T_{max}$ at ~577 °C. This higher intensity is due to increased hydrogen consumption which can be attributed to reaction of surface sulfate species present on the used catalyst with hydrogen. The reduction of iron sulfate proceeds in hydrogen atmosphere giving hydrogen sulfide [52,53], and if we consider Eq. (7) as the reduction phenomenon then we see that for 1 mole of ferric sulfate to reduce completely to iron, 15 mole of hydrogen will be consumed (Eqs. (4)–(7)) in contrast to 3 mole of hydrogen for reduction of 1 mole of $Fe_2O_3$ to Fe (Eqs. (4)–(6)).

$$3Fe_2O_3 + H_2 = 2Fe_3O_4 + H_2O \quad (4)$$

$$2Fe_3O_4 + 2H_2 = 6FeO + 2H_2O \quad (5)$$

$$6FeO + 6H_2 = 6Fe + 6H_2O \quad (6)$$

$$Fe_2(SO_4)_3 + 12H_2 = Fe_2O_3 + 3H_2S + 9H_2O \quad (7)$$

The spent catalyst was also subjected to an evolved gas analysis (EGA) experiments as a function of temperature. The evolved gases were detected using a quadruple mass spectrometer. Since the spent catalyst was having surface sulfate species, we attempted to track the decomposition profile of this surface sulfate. Ferric sulfate decomposes at higher temperature to form $SO_2$ and the formation and decomposition of this sulfate was proposed to be the most probable mechanism in our earlier study [28]. Iron oxide catalyst on exposure to $SO_3$ vapors will form surface sulfate species, but if the temperature of the iron oxide catalyst is higher than the decomposition temperature of iron sulfate, the sulfate becomes a metastable phase and the sulfate will rapidly decompose to form $SO_2$. Thus $SO_3$ decomposition to $SO_2$ is proposed to follow this concerted mechanism of surface metal sulfate formation and decomposition. The formation of bulk ferric sulfate and its decomposition can be represented by Eqs. (8) and (9) respectively.

$$Fe_2O_3 + 3SO_3 = Fe_2(SO_4)_3 \quad (8)$$

$$Fe_2(SO_4)_3 = Fe_2O_3 + 3SO_2 + 1.5O_2 \quad (9)$$

The temperature of formation of this $SO_2$ as a decomposition product from sulfate species was determined from the EGA of the spent catalysts. A plot of intensity of evolved gas, having mass number 64 ($SO_2$), in the temperature range of 250–1000 °C is shown in Fig. 8. EGA analysis revealed that both the spent catalysts evolve $SO_2$ as a decomposition product of its sulfate as the temperature is increased and the pattern of decomposition is similar. It is evident that the $T_{max}$ (temperature at which maximum $SO_2$ was evolved) is

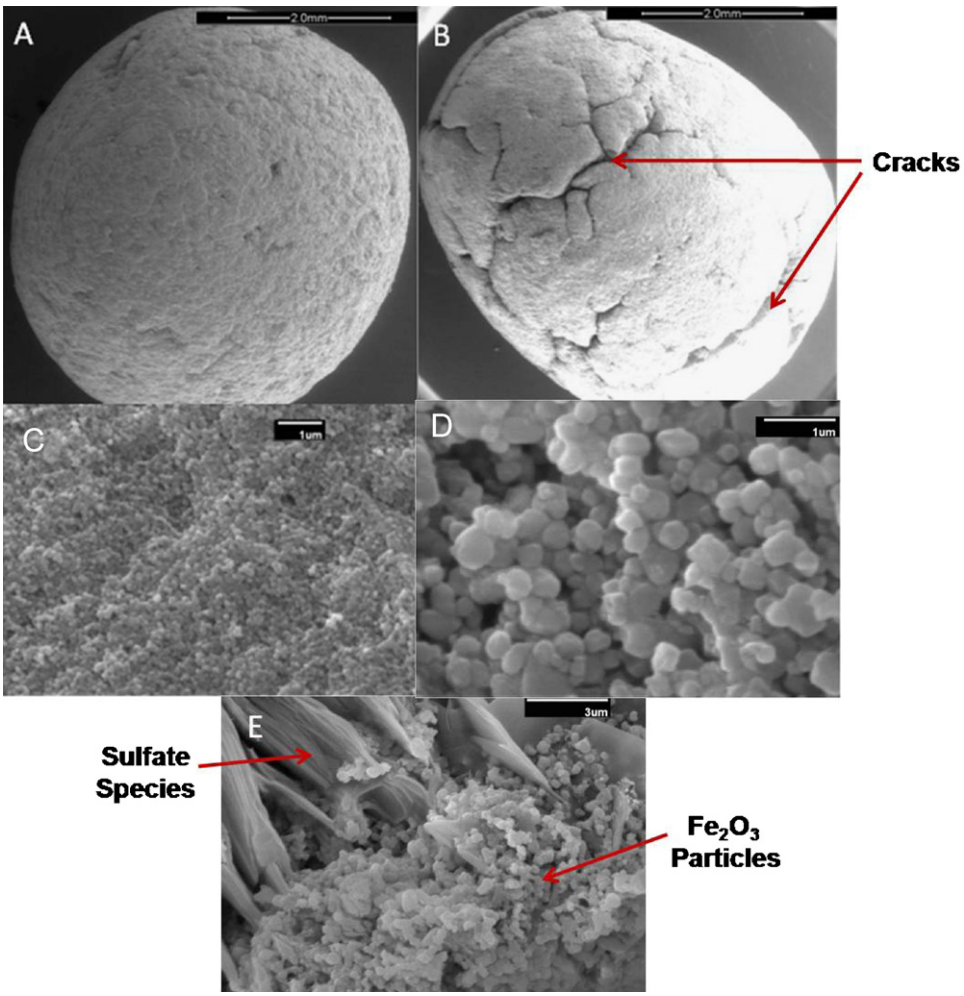


**Fig. 9.** Scanning Electron Micrographs of fresh and spent $Fe_2O_3$ catalysts: (A and C) before reaction and (B, D, and E) after 100 h use in sulfuric acid decomposition reaction.

lower in case of Cr-doped iron oxide ($Fe_{1.8}Cr_{0.2}O_3$) suggesting facile decomposition of sulfate on this sample. Appearance of broader $SO_2$ evolution peak in the EGA of spent $Fe_2O_3$ than on spent $Fe_{1.8}Cr_{0.2}O_3$ further suggested slower kinetics of decomposition of sulfate on former sample. Another interesting observation which is evident from the EGA curves is that the amount of $SO_2$ evolved is much higher in case of $Fe_{1.8}Cr_{0.2}O_3$ that $Fe_2O_3$.

The microstructure evolution during this 100 h reaction process can be observed in Fig. 9 by the Scanning Electron Micrograph of the fresh and used $Fe_2O_3$ catalyst spherical granules. Fig. 9A shows the clean spherical $Fe_2O_3$ surface of the unused pellet having a diameter of ~5 mm while Fig. 9B exhibits the development of cracks on the surface of the spherical catalyst granules as a result of catalyzing the high temperature sulfuric acid decomposition for 100 h. The SEM micrograph of pristine $Fe_2O_3$ sample prepared by precipitation method and calcined at 750 °C shows mono-dispersed spherical particles of $Fe_2O_3$ with a size ~100 nm (Fig. 9C). The grain boundaries are also visible in this micrograph. Agglomeration and grain growth are evident from Fig. 9C and D, where we observe that the ~100 nm particles in the fresh catalyst grows to 250–500 nm in the used one. Fig. 9E shows the SEM of the used $Fe_2O_3$ catalyst inside the cracked site. Although, agglomerated particles of iron oxide were visible on majority of the surface of the used catalyst (as was obvious in Fig. 9D), Fig. 9E shows that at a certain location numerous needle shaped crystals which can be attributed to the formation of ferric sulfate species. The specific location shown in Fig. 9E is near a crack portion of the spherical pellet where we clearly observe the growth of ferric sulfate crystals over the agglomerated ferric oxide particles. The microstructural characteristics were similar in the chromium doped samples. Fig. 10 shows the morphology of the fresh and spent $Fe_{1.8}Cr_{0.2}O_3$ catalysts surfaces. Similar to iron oxide the SEM micrographs of $Fe_{1.8}Cr_{0.2}O_3$ (Fig. 10A) shows monodisperse spherical particles of size in the range of ~100 nm with prominent grain boundaries while grain growth is clearly evident in the spent catalyst (Fig. 10B) where agglomerated particles of larger size are observed. Fig. 10C shows elongated sulfate crystals at a cracked site on the surface of the catalyst pellet. From SEM studies it can be concluded that particle agglomeration is a major phenomenon occurring on the spent catalyst surface during 100 h catalytic runs at high temperature of ~800 °C. Also, formation of elongated concentrated crystals at surface sites were evident in small concentration, i.e., discontinuity of sulfate concentration exist all over the catalyst surface.From the SEM micrographs of the spent catalysts it is evident from that particle agglomeration due to sintering at high temperature is more severe on the pristine sample. For both the fresh catalysts the average particle size were ~100 nm which increased to ~200–400 nm (majority of particles) in the spent $Fe_2O_3$ in comparison to ~150–300 nm in the doped sample. Thus, presence of chromium helps in prevention of sintering in $Fe_2O_3$ which was observed from our TPR results in our earlier study [29]. This phenomenon is similar to that observed in chromium doped iron oxide catalysts in water gas shift reaction where sintering is minimized by similar amounts of Cr present in the active phase $Fe_3O_4$ [54,55]. Thus, it is expected that the

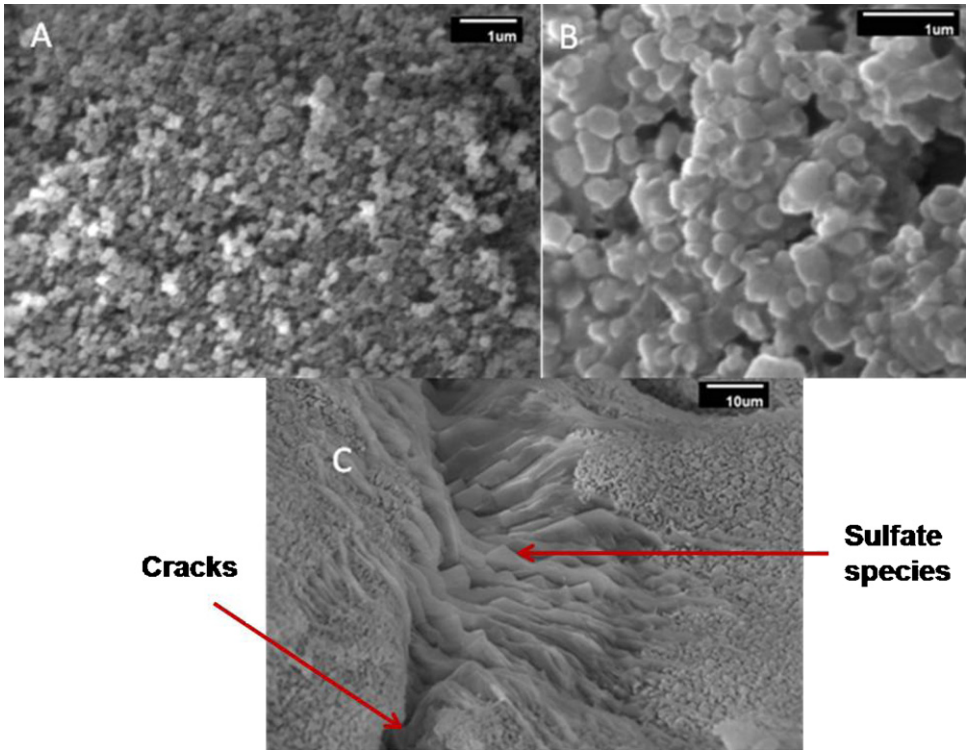


**Fig. 10.** Scanning Electron Micrographs of fresh and spent $Fe_{1.8}Cr_{0.2}O_3$: (A) before reaction and (B and C) after 100 h use in sulfuric acid decomposition reaction.

formation of surface sulfate might play a role in the larger decrease in the BET surface area of the spent catalyst in case of $Fe_{1.8}Cr_{0.2}O_3$. In this regard we would like to refer the FTIR spectra of the used catalysts in Fig. 4, from where it is evident that the intensity of the sulfate species is more on the doped catalysts indicating the presence of sulfates in higher amounts in the doped catalyst. This fact was further confirmed by our evolved gas analysis results (Fig. 8) which showed grater evolution of $SO_2$ from the doped catalyst than the pristine one. Thus, from the SEM, FTIR, and EGA results we can infer that the larger decrease in BET surface area of spent $Fe_{1.8}Cr_{0.2}O_3$ sample than $Fe_2O_3$ is primarily due to surface sulfate formation. Such a decrease in $N_2$-BET surface area on sulfation of oxide catalysts has been reported by several authors over various oxides viz. iron-chromium oxide clay [56], ceria–zirconia [57], $TiO_2$ [58], dolomite [59], and iron titanates [60].

From the ex situ analysis of the spent catalyst samples we can have an insight into the mechanism of the high temperature sulfuric acid decomposition reaction. Lack of in situ instrumentation facilities at high temperature and corrosive environments makes the prediction of the reaction mechanism difficult. We have discussed in our previous publication [29] that a metal sulfate formation and decomposition route can be a plausible mechanism for the $SO_3$ decomposition on iron and chromium doped iron oxides. Further, our recent investigation [28] with ferrospinel catalysts for sulfuric acid decomposition helped us to propose a three step model for the decomposition reaction over metal oxides. From the spent catalyst investigations carried out in this work, we further improvise upon our previous suggestion regarding the most probable mechanism over iron oxide based catalysts [29]. From the spent catalyst investigations carried out in this work, it can be said that on use for sulfuric acid decomposition reaction, iron oxide catalyst showed evidence of formation of metal sulfates on the surface which again undergoes thermal decomposition producing $SO_2$. Thus $SO_3$ decomposition to $SO_2$ can be proposed to follow this concerted mechanism of surface metal sulfate formation and decomposition. The most probable mechanism of sulfuric acid decomposition over the iron oxide catalysts is shown in Scheme 2 (Eqs. (10)–(12)). The surface of a stoichiometric oxide is shown in the reactant side of Eq. (10). Transition metal oxides like $Fe_2O_3$ are generally n-type semiconductors which lose lattice oxygen on heating, causing anionic vacancies [29,61,62], thus oxygen vacant site are available on the catalyst surfaces at high temperatures. These oxygen surface oxygen deficient sites acts as active sites in $Fe_2O_3$ catalyst even for Fischer–Tropsch synthesis [62] or CO-oxidation [63]. This process requires a reduction of the metal cations i.e., $Fe^{3+} \Leftrightarrow Fe^{2+}$ to maintain electroneutrality in the system. Thus the redox properties of the iron oxides play a crucial role in determining the kinetics of this step. From the TPR results in our earlier publication [28] we observed that the solid solution of 10 at.% Cr substitution in $Fe_2O_3$ lattice has not only eased the reducibility of $Fe^{3+}$ in $Fe_2O_3$ but also enhanced reproducibility toward repeated reduction–oxidation cycles. Thus working of the redox couple $Fe^{3+} \Leftrightarrow Fe^{2+}$ is more facile in the chromium doped sample. Next, a $SO_3$ molecule interacts with such a surface active site ([*]) which are the oxygen vacant site on the metal oxide surface to form a bidentate surface sulfate species as shown in Eq. (11) in Scheme 2. This $SO_3$ comes from the thermal dehydration of sulfuric acid at high temperature (>450 °C) (Eq. (1)). It is important to notice here that out of the four oxygens in a surface sulfate species three came from $SO_3$ and one from the metal oxide. The sulfate then undergoes decomposition producing $SO_2$ and the stoichiometric metal oxide as shown in Eq. (12). The reduced metal (M) centers will be subsequently oxidized by the reduction of $SO_3$ to $SO_2$. Again, the redox couples $M^{x+} \Leftrightarrow M^{(x-1)+}$, e.g., $Fe^{3+} \Leftrightarrow Fe^{2+}$ plays a crucial role here.

From the temperature dependent catalytic activity (Fig. 2a) we can clearly see that at lower temperatures <775 °C, the catalytic activity of the doped sample is much higher than the undoped $Fe_2O_3$. At higher temperatures >775 °C the catalytic curves for the two oxide is similar in shape with the doped catalyst showing slightly higher activity as compared to the pristine $Fe_2O_3$. The metal sulfate formation and decomposition (Eqs. (11) and (12) in Scheme 2) over iron oxide catalysts involves the working of the vital

Step 1:Loss of lattice oxygen at high temperatures (Reduction of Surface); facilitated by $Fe^{3+} \leftrightarrow Fe^{2+}$ redox couple


.....(10)

Step 2: Surface Sulfate Formation (partial oxidation of surface and initiation of reduction of $SO_3$);

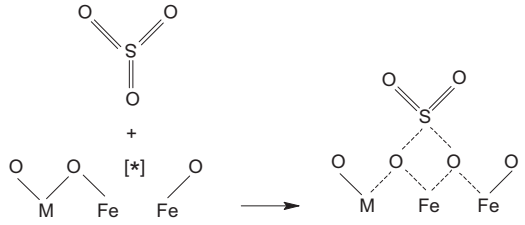


.....(11)

Step 3: Surface Sulfate Deomposition (complete oxidation of surface and evolution of $SO_2$ by complete reduction of $SO_3$); facilitated by low thermal stability of metal sulfate and the $Fe^{3+} \leftrightarrow Fe^{2+}$ redox couple

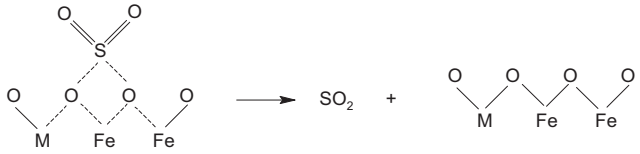


.....(12)

**Scheme 2.** A schematic presentation of proposed most probable mechanism for sulfuric acid decomposition over iron oxide (undoped and doped) catalysts. [*] denotes surface active sites.

redox couple $Fe^{3+} \Leftrightarrow Fe^{2+}$. In addition to this fact, our EGA results show (Fig. 8) the facile decomposition of the sulfate present on the used catalyst of the substituted oxide which definitely suggests the faster kinetics of the decomposition step (Eq. (12) in Scheme 2). The lesser thermal stability of the sulfate of the chromium substituted iron oxide imparts faster sulfate decomposition rate. Due to very fast mobility of lattice oxygen, the generation of surface oxide ion vacancies in these oxides (Eq. (10) in Scheme 2) at very high temperatures (>800 °C) will be comparable and shall have very little kinetic implication. Thus the metal sulfate formation and decomposition will play the most crucial role in determination of kinetics of sulfuric acid decomposition. From the standpoint of better redox properties and the inferior thermal stability of sulfate the chromium substituted iron oxide stands superior to pristine iron oxide regarding catalytic performance on both the sulfate formation and decomposition steps. Thus, the Cr-doped $Fe_2O_3$ is found to be more active catalyst which is ascribed to its lower thermal stability of its sulfate, and improved redox properties. However, both the catalysts were found to be maintaining its catalytic activity for 100 h indicating that the oxide catalysts are stable under the harsh reaction environment.

## 4. Conclusion

Our results show that both $Fe_2O_3$ and Cr-doped $Fe_2O_3$ are active formulations for sulfuric acid decomposition without showing any visible deactivation. These catalysts have potential for their practical applicability at enhanced scale. 20 g of spherical granule macroparticles of both the catalysts, viz.; $Fe_2O_3$ and 10% Cr doped $Fe_2O_3$, were tested in quartz reactor which is an integrated acid boiler, preheater, and decomposer (bayonet type). The performances of catalysts were monitored as a function of time, temperature, and acid flow rates. No decrease in catalytic activity was observed for either catalyst during a 100 h catalytic run at 800 °C and at an acid flux of 0.63 ml $min^{-1}$, but the chromium doped sample exhibited slightly higher catalytic activity over the entire time period. The enhanced catalytic activity of chromium doped $Fe_2O_3$ was ascribed to the lower thermal stability of its sulfate and improved redox properties.

## Acknowledgments

The authors thank Dr. Tulsi Mukherjee, Director, Chemistry Group, BARC, for his constant support and encouragement during the entire course of this work. The authors also thank Shri. Siddhartha Kolay and Shri. N. Manoj of Chemistry Division, BARC, for recording the EGA runs and SEM images, respectively and Mr. Jagannath of TPD, BARC, for recording the XPS spectra.

## References

[1] D. O'Keefe, C. Allen, G. Besenbruch, L. Brown, J. Norman, R. Sharp, K. McCorkle, International Journal of Hydrogen Energy 7 (1982) 381–392.
[2] L.E. Brecher, S. Spewock, C.J. Warde, International Journal of Hydrogen Energy 2 (1977) 7–15.
[3] G.E. Beghi, International Journal of Hydrogen Energy 11 (1986) 761–771.
[4] M.A. Pena, J.P. Gomez, J.L.G. Fierro, Applied Catalysis A: General 144 (1996) 7–57.
[5] P. Favuzza, C. Felici, L. Nardi, P. Tarquini, A. Tito, Applied Catalysis B: Environmental 105 (2011) 30–40.
[6] K. Onuki, S. Kubo, A. Terada, N. Sakaba, R. Hino, Energy and Environmental Science 2 (2009) 491–497.
[7] C.E. Bamberger, D.M. Richardson, Cryogenics 16 (1976) 197–208.
[8] S. Kubo, H. Nakajima, S. Kasahara, S. Higashi, T. Masaki, H. Abe, K. Onuki, Nuclear Engineering and Design 233 (2004) 347–354.
[9] S. Brutti, G. De Maria, G. Cerri, A. Giovannelli, B. Brunetti, P. Cafarelli, E. Semprin, V. Barbarossa, A. Ceroli, Industrial & Engineering Chemistry Research 46 (2007) 6393–6400.
[10] C. Huang, A. T-Raissi, Solar Energy 78 (2005) 632–646.
[11] D.R. Okeefe, J.H. Norman, D.G. Williamson, Catalysis Reviews: Science and Engineering 22 (1980) 325–369.
[12] D.M. Ginosar, L.M. Petkovic, A.W. Glenn, K.C. Burch, International Journal of Hydrogen Energy 32 (2007) 482–488.
[13] L.M. Petkovic, D.M. Ginosar, H.W. Rollins, K.C. Burch, P.J. Pinhero, H.H. Farrell, Applied Catalysis A 338 (2008) 27–36.

[14] B.M. Nagaraja, K.D. Jung, B.S. Ahn, H. Abimanyu, K.S. Yoo, Industrial and Engineering Chemistry Research 48 (2009) 1451–1457.
[15] S.N. Rashkeev, D.M. Ginosar, L.M. Petkovic, H.H. Farrell, Catalysis Today 139 (2009) 291–298.
[16] J.H. Norman, K.J. Mysels, R. Sharp, D. Williamson, International Journal of Hydrogen Energy 7 (7) (1982) 545–556.
[17] M. Dokiya, T. Kameyama, K. Fukuda, Y. Kotera, Bulletin of the Chemical Society of Japan 50 (1977) 2657–2660.
[18] H. Tagawa, T. Endo, International Journal of Hydrogen Energy 14 (1989) 11–17.
[19] V. Barbarossa, S. Brutti, M. Diamantia, S. Saua, G. De Mariab, International Journal of Hydrogen Energy 31 (2006) 883–890.
[20] G. Busca, L. Lietti, G. Ramis, F. Berti, Applied Catalysis B: Environmental 18 (1998) 1–36.
[21] R. Burch, J.P. Breen, F.C. Meunier, Applied Catalysis B: Environmental 39 (2002) 283–303.
[22] M.R. Pai, A.M. Banerjee, K. Karha, R.V. Pai, V.S. Kamble, S.R. Bharadwaj, Journal of Physical Chemistry B 114 (2010) 6943–6953.
[23] F. Huber, J. Walmsley, H. Venvik, A. Holmen, Applied Catalysis A: General 349 (2008) 46–54.
[24] L.N. Yannopoulos, J.F. Pierre, International Journal of Hydrogen Energy 9 (5) (1984) 383–390.
[25] T.-H. Kim, G.-T. Gong, B.G. Lee, K.-Y. Lee, H.-Y. Jeon, C.-H. Shin, H. Kim, K.-D. Jung, Applied Catalysis A: General 305 (2006) 39–45.
[26] D.M. Ginosar, H.W. Rollins, L.M. Petkovic, K.C. Burch, M.J. Rush, International Journal of Hydrogen Energy 34 (2009) 4065–4073.
[27] M. Machida, Y. Miyazaki, Y. Matsunaga, K. Ikeue, Chemical Communications 47 (2011) 9591–9593.
[28] A.M. Banerjee, M.R. Pai, S.S. Meena, A.K. Tripathi, S.R. Bharadwaj, International Journal of Hydrogen Energy 36 (2010) 4768–4780.
[29] A.M. Banerjee, M.R. Pai, K. Bhattacharya, A.K. Tripathi, V.S. Kamble, S.R. Bharadwaj, S.K. Kulshreshtha, International Journal of Hydrogen Energy 33 (2008) 319–326.
[30] G.C. Bond, Principles of Catalysis, London Chemical Society, London, 1972.
[31] T. Takai, S. Kubo, T. Nakagiri, Y. Inagak, International Journal of Hydrogen Energy 36 (2011) 4689–4701.
[32] N. Sakaba, S. Kasahara, K. Onuki, K. Kunitomi, International Journal of Hydrogen Energy 32 (2007) 4160–4169.
[33] F. Castellino, S.B. Rasmussen, A.D. Jensen, J.E. Johnsson, R. Fehrmann, Applied Catalysis B: Environmental 83 (2008) 110–122.
[34] Y. Zheng, A.D. Jensen, J.E. Johnsson, J.R. Thøgersen, Applied Catalysis B: Environmental 83 (2008) 186–194.
[35] T. O'Doherty, A.J. Jolly, C.J. Bates, Applied Thermal Engineering 21 (2001) 1–18.
[36] V. Nagarajan, V. Ponyavin, Y. Chen, M.E. Vernon, P. Pickard, A.E. Hechanov, International Journal of Hydrogen Energy 33 (2008) 6445–6455.
[37] V. Nagarajan, V. Ponyavin, Y. Chen, M.E. Vernon, P. Pickard, A.E. Hechanova, International Journal of Hydrogen Energy 34 (2009) 2543–2557.
[38] T. Ma, M. Zeng, Y. Ji, H. Zhu, Q. Wang, International Journal of Hydrogen Energy 36 (2011) 3757–3768.
[39] T. Ma, Y.-t. Chen, M. Zeng, Q.-w. Wang, Applied Thermal Engineering 43 (2012) 101–108.
[40] V.S. Jakkal, private communication.
[41] F. Magalhaes, M.C. Pereira, S.E.C. Botrel, J.D. Fabris, W.A. Macedo, R. Mendonc, R.M. Lago, L.C.A. Oliveira, Applied Catalysis A: General 332 (2007) 115–123.
[42] Handbook of X-ray Photoelectron Spectroscopy, Perkin-Elmer Corp., Physical Electronics Division, New York, 1992.
[43] D.R. Milburn, R.A. Keogh, R. Srinivasan, B.H. Davis, Applied Catalysis A: General 147 (1996) 109–125.
[44] S. Richardson, D.J. Vaughan, Mineralogical Magazine 53 (April) (1989) 223–229.
[45] D.R. Milburn, R.A. Keogh, D.E. Sparks, B.H. Davis, Applied Surface Science 126 (1998) 11–15.
[46] N.T. McDevitt, W.L. Baun, Spectrochimica Acta 20 (1964) 799.
[47] U. Schwertmann, R.M. Taylor, Minerals in Soil Environments, Soil Science Society of America, Inc., Madison, WI, 1977, p. 145.
[48] K.K. Kartha, M.R. Pai, A.M. Banerjee, R.V. Pai, S.S. Meena, S.R. Bharadwaj, Journal of Molecular Catalysis A 335 (2011) 158–168.
[49] J.D. Kubicki, K.W. Paul, D.L. Sparks, Geochemical Transactions 9 (2008) 4.
[50] S.J. Hug, Journal of Colloid and Interface Science 188 (1997) 415–422.
[51] S.K. Samantaray, K.M. Parida, Journal of Materials Science 38 (2003) 1835–1848.
[52] L. Ma, J. Li, R. Ke, L. Fu, Journal of Physical Chemistry C 115 (2011) 7603–7612.
[53] J.D. Henao, B. Wen, W.M.H. Sachtler, Journal of Physical Chemistry B 109 (2005) 2055–2063.
[54] H. Topsoe, J.A. Dumesic, M. Boudart, Journal of Catalysis 28 (1973) 477.
[55] A. Khan, P. Chen, P. Boolchand, P.G. Smirniotis, Journal of Catalysis 253 (2008) 91–104.
[56] T. Mishra, K.M. Parida, Journal of Colloid and Interface Science 301 (2006) 554.
[57] L. Zhang, D. Weng, B. Wang, X. Wu, Catalysis Communications 11 (2010) 1229.
[58] Z. Ma, Y. Yue, X. Deng, Z. Gao, Journal of Molecular Catalysis A: Chemical 178 (2002) 97.
[59] I. Ávila, P.M. Crnkovic, F.E. Milioli, K.H. Luo, Applied Surface Science 258 (2012) 3532.
[60] F. Liu, K. Asakura, H. He, W. Shan, X. Shi, C. Zhang, Applied Catalysis B: Environmental 103 (2011) 369–377.
[61] X. Yang, L. Li, Nanotechnology 21 (2010) 355602.
[62] S. Li, W. Ding, G.D. Meitzner, E. Iglesia, Journal of Physical Chemistry B 106 (2002) 85–91.
[63] S. Wagloehner, D. Reichert, D. Leon-Sorzano, P. Balle, B. Geiger, S. Kureti, Journal of Catalysis 260 (2008) 305–314.